Old Dominion University

ODU Digital Commons

2021

Magnetic Field Sensors for Detection of Trapped Flux in Superconducting Radio Frequency Cavities

Ishwari Prasad Parajuli
Old Dominion University, iparajul@odu.edu

Gianluigi Ciovati
Old Dominion University, gciovati@odu.edu

Jean R. Delayen
Old Dominion University, jdelayen@odu.edu

Follow this and additional works at: https://digitalcommons.odu.edu/physics_fac_pubs

Part of the Electromagnetics and Photonics Commons, Elementary Particles and Fields and String Theory Commons, and the Engineering Physics Commons

Original Publication Citation

Magnetic field sensors for detection of trapped flux in superconducting radio frequency cavities

View Online   Export Citation   CrossMark

I. P. Parajuli,[1] (ID) G. Ciovati,[1,2,a] (ID) and J. R. Delayen[1,2] (ID)

AFFILIATIONS

[1] Center for Accelerator Science, Department of Physics, Old Dominion University, Norfolk, Virginia 23529, USA
[2] Thomas Jefferson National Accelerator Facility, Newport News, Virginia 23606, USA

[a] Author to whom correspondence should be addressed: gciovati@jlab.org

ABSTRACT

Superconducting radio frequency (SRF) cavities are fundamental building blocks of modern particle accelerators. They operate at liquid helium temperatures (2–4 K) to achieve very high quality factors (10^{10}–10^{11}). Trapping of magnetic flux within the superconductor is a significant contribution to the residual RF losses, which limit the achievable quality factor. Suitable diagnostic tools are in high demand to understand the mechanisms of flux trapping in technical superconductors, and the fundamental components of such diagnostic tools are magnetic field sensors. We have studied the performance of commercially available Hall probes, anisotropic magnetoresistive sensors, and flux-gate magnetometers with respect to their sensitivity and capability to detect localized, low magnetic flux amplitudes, of the order of a few tens of magnetic flux quantum at liquid helium temperatures. Although Hall probes have the lowest magnetic field sensitivity (~ 96 nV/μT at 2 K), their physical dimensions are such that they have the ability to detect the lowest number of trapped vortices among the three types of sensors. Hall probes and anisotropic magnetoresistive sensors have been selected to be used in a setup to map regions of trapped flux on the surface of a single-cell SRF cavity.

Published by AIP Publishing. https://doi.org/10.1063/5.0063177

I. INTRODUCTION

Superconducting radio frequency (SRF) cavities are fundamental components of modern particle accelerators, providing efficient acceleration of charged particle beams. Ideally, SRF cavities should operate in the vortex-free Meissner state when cooled below their critical temperature, T_c. However, the unavoidable presence of defects in large-size (volume greater than ~ 300 cm^3) technical superconductors results in a state in which bundles of vortices, each carrying the magnetic flux quantum ϕ_0, get trapped in a superconductor upon its cooling through T_c. Oscillation of pinned vortex segments under the RF field at the inner surface of SRF cavities results in residual losses limiting their quality factor and therefore their efficiency at liquid helium temperatures. This issue is well-known, and it is mitigated by enclosing SRF cavities inside one or more magnetic shields to screen the ambient field, such as the Earth's magnetic field, down to a practical limit of a few milligauss.[1] However, even such a low residual magnetic field can result in vortices spaced by a few tens of micrometers, producing losses of the order of a few nano-Ohm at gigahertz frequencies. Such losses are of the same order as the quasiparticle RF losses described by the

Bardeen–Cooper–Schrieffer (BCS) theory of superconductivity[2,3] or even dominate the RF losses in lower frequency cavities. As more efficient, lower cost particle accelerators are being sought after and developed, significant research and development efforts, both theoretical[4–9] and experimental,[10–16] have been devoted in recent years to understanding the mechanisms of flux trapping, their contribution to the RF losses, and methods to reduce the amount of trapped flux.

Scanning imaging techniques have been successfully developed to investigate vortices in superconductors; however, they are applied to small, cm^2-sized, flat, smooth samples.[17] On the other hand, the investigation of trapped flux in SRF cavities is best done on a "subunit" of a real SRF accelerating structure, such as a single-cell cavity, which has been subjected to the same complex metallurgical and surface processing steps as the cavities installed in particle accelerators.[1] Each of the cavity processing steps can affect the size, density, and distribution of pinning centers. The typical single-cell cavity used for SRF research has a surface area of ~ 1000 cm^2, and it has a curved profile and a root mean square surface roughness of the order of 500 nm.

In order to identify and study trapped flux in SRF cavities, it would be valuable to develop a diagnostic tool, capable of detecting

magnetic vortices trapped in the cavity wall upon cooldown across T_c, as a function of different relevant parameters, such as the cavity material and treatments, temperature gradients during cooldown, and amplitude and direction of the residual magnetic field. A magnetic field scanning system (MFSS) for 1.3 GHz single-cell SRF cavities is being developed at Old Dominion University and Jefferson Lab for this purpose.[18] The setup is designed to hold two types of magnetic field sensors, which could be complementary in terms of magnetic field sensitivity and spatial resolution. Three types of sensors have been considered: cryogenic Hall probe (HP), anisotropic magnetoresistive (AMR) sensor, and cryogenic flux-gate magnetometer (FGM). This article presents results for each type of sensor related to their magnetic field sensitivity, the resolution of the data acquisition system used for the sensors' readout, and the potential ability to detect trapped magnetic flux on the cavity surface.

II. MAGNETIC FIELD SENSORS

A. Cryogenic Hall probe

A single-axis, high-linearity cryogenic Hall probe, model HHP-VFS from AREPOC, Slovakia, was considered for the MFSS. The sensor has an active area of 50×50 μm, and it measures the field component perpendicular to the sample surface at 120 μm distance. The sensor is designed to operate in a magnetic field of up to 5 T between 1.5 and 350 K, and it is packaged in a cylindrical housing, 7 mm in diameter, 8 mm long. Additional sensor specifications are: an offset voltage of less than 200 μV, with a temperature coefficient of less than 0.3 μV/K, a sensitivity, S, greater than 50 mV/T at the nominal current of 10 mA, with a temperature coefficient of 5×10^{-5} K^{-1} between 4.2 and 77 K, and a linearity error of less than 1.5% at 4.2 K, between 0 and 5 T.[19] Figure 1 shows an image of the sensor's active area.

B. Anisotropic magnetoresistive sensor

AMR sensors are used in many applications, such as navigation, non-destructive evaluation, and vehicle detection.[20-23] Two single-axis AMR sensors, model HMC1001 from Honeywell International,

FIG. 1. Optical microscopy image of the active area of the Hall probe sensor HHP-VFS.

USA, and model AFF755B from Sensitec, Germany, have been studied for measuring the residual magnetic field on superconducting samples at liquid helium temperatures.[24] The sensor from Sensitec has been recently extensively characterized[25,26] and used to detect the residual magnetic field near the surface of SRF cavities,[27-30] so we selected this sensor to be evaluated for use in the MFSS. Some of the sensor specifications at room temperature are: a power supply voltage V_{dc} between 1.2 and 9 V, a typical sensitivity S/V_{dc} of 12 mV/mT/V, an offset voltage of ± 0.5 mV/V, and a linearity error of 0.15% of full-scale in the range ± 100 μT.[31] The sensor has an active area of 0.7×0.8 mm^2, and it is packaged into an integrated circuit with overall dimensions of 4.9 mm length, 3.8 mm width, and 1.75 mm height. A flip coil, used to align the ferromagnetic sensing elements to an easy magnetization axis, and a test coil to check the sensor's response are also part of the integrated circuit.

C. Cryogenic fluxgate magnetometer

A single-axis cryogenic fluxgate magnetometer, model Mag-F from Bartington Instruments, UK, was also considered for use in the MFSS. This sensor is routinely used to measure the residual magnetic field near the surface of SRF cavities, and a 1 mm diameter and 28 mm long active area is enclosed in a 6 mm diameter and 32 mm long cylindrical body. The sensor's range is ± 200 μT. A nanotesla-meter (Mag-01H, Bartington Instruments, UK) is used in conjunction with the FGM and has a resolution of 0.1 nT between 0 and 2 μT and 1 nT in the range 2–100 μT. The offset in zero field is specified to be ± 5 nT at 20 °C with a temperature coefficient of 0.01 nT/°C.[32] The nanotesla-meter also has an analog output with a 100 mV/μT scaling.

III. EXPERIMENTAL RESULTS

A. Sensor calibration

Figure 2 shows a picture of the three types of sensors being evaluated. The sensors to be calibrated are placed inside a set of Helmholtz coils (model 1000906, 3B Scientific, USA, 300 mm mean coil diameter, 150 mm mean coil spacing, 740 μT/A) aligned to the direction of the uniform field inside the coils, along with one FGM, used as a reference sensor. The experimental setup is mounted on a vertical test stand inserted in a Dewar filled with liquid helium. A power supply (model 2400, Keithley Instruments, USA) is connected to the Helmholtz coils. A 24-bit voltage input data acquisition module (NI-9239, National Instruments, USA) is used to measure the analog voltage output of the Mag-01H, connected to the FGM. For the calibration of the HP, an 8-channel, 24-bit data acquisition module (USB2AD, AREPOC, Slovakia) was used to supply the nominal current and read the sensors' voltage, whereas a 16-channel data acquisition unit (model 2701 digital multimeter with a model 7701 low-voltage multiplexer, Keithley Instruments, USA) was used to measure the voltage from the AMR sensors. A pulsed DC source (model 2611, Keithley Instruments, USA) is used to drive the flip coil of the AMR sensors, and a power supply voltage of 5 V was applied to the sensors using a standard AC–DC power adapter. The instrument control and data acquisition were performed using programs written in LabVIEW.[33]

16 HP and 32 AMR sensors were calibrated. The sensor calibration procedure consists of measuring the sensors' voltage, V,
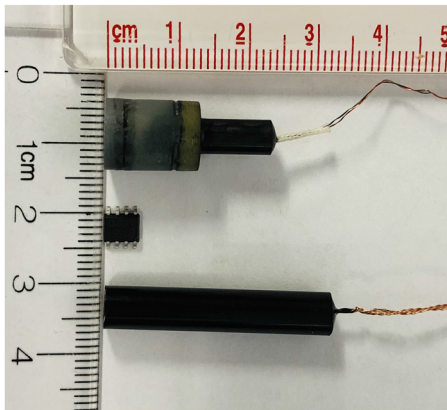
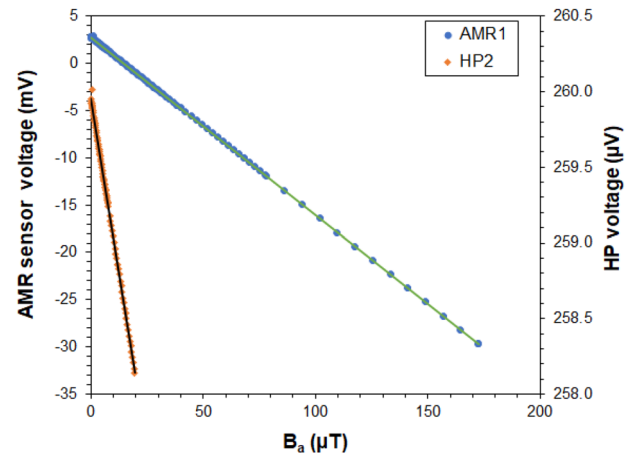**FIG. 2.** Picture of a HP (top), AMR sensor (middle), and FGM (bottom).

FIG. 3. Sensor voltage as a function of the applied magnetic field for one HP and one AMR sensor. Solid lines are a linear least-square fit to each set of data.

as a function of the applied magnetic field, B_a, in the range ± 200 mG, starting from ~ 2 mG: the slope of the $V(B_a)$ plot is the sensor sensitivity, S, and the intercept is the offset voltage, V_0. For the HP calibration, the nominal current of 10 mA was applied to the sensors, and the USB2AD data acquisition module allows for the chopping technique to be applied on either analog inputs or analog outputs.[34] The chopping technique consists of switching the direction of the bias current and measuring the average sensor voltage, allowing eliminating spurious offset voltages in the circuit of the sensor connection. Measurements were performed with chopping for 20 cycles on the analog output, and each data point was the average of four samples. In the case of the AMR sensors, each $V(B_a)$ data point was the average of four measurements and the calibration was performed in two ways: In the first case, a 100 ms long pulse of 150 mA was applied to the flip coil before each data point, and in the second case, the pulse was only applied at the beginning of the entire calibration. In both cases, the flip coil pulse was applied at the calibration temperature, below 40 K. The average sensitivity measured in the first case was 34.4 ± 0.5 μV/μT/V, whereas it was 35.6 ± 0.6 μV/μT/V in the second case. The HP sensor calibration was performed at three temperatures: 2, 4.3, and ~ 9.5 K, and the calibration of the AMR sensors was performed at 2, 4.3, 14, and 35 K. Figure 3 shows a plot of $V(B_a)$ for one of the AMR and HP sensors. Table I shows a summary of the sensitivity, offset voltage, linearity error, and temperature coefficients for the AMR and HP sensors. The average sensitivity of the AMR sensors at 2 K with a single flip coil pulse is consistent with that reported in Ref. 25.

The stability of the sensitivity of the AMR sensors with respect to thermal cycling was evaluated by subjecting a set of 16 sensors to 35 thermal cycles between 77 and 300 K and five additional thermal cycles between 4.3 and 300 K, prior to repeating the sensor calibration. The results showed that the average change in sensitivity was 0.5%–2% between 2 and 10 K.

A calibration of the fluxgate magnetometers was not required; however, an experiment was performed to verify the ability of the sensor to measure a non-uniform field, over its length. To perform the experiment, a NdFeB cylindrical permanent magnet 25.4 mm long, 1.25 mm diameter (D1X0, K & J Magnetics, USA) was placed on a wooden block and a flux-gate magnetometer was placed on another wooden block, with its axis aligned to the axis of the permanent magnet. The magnetic field was measured with the Mag-01H nanotesla-meter as a function of the distance between the tip of the magnet and the tip of the sensor's core. The measurements were taken in a shielded room with a background magnetic field of ~ 1 μT, which was subtracted from the data. Figure 4 shows the magnitude of the magnet axial magnetic field as a function of the distance from the magnet tip, provided by the vendor, the magnetic field measured by the FGM, and the magnet field averaged over the 28 mm length of the FGM's core, at the measured position. The data show that the magnetic field measured by the FGM is consistent with the average field over the core's length.

TABLE I. Average values of HP and AMR sensor parameters obtained from the calibration of 16 HP and 32 AMR sensors, in the range 2–9 K and 0–195 mG for HP, and in the range 2–35 K and 0–1800 mG for AMR sensors. For the AMR sensors, the range of offset voltage values and their temperature coefficients are reported because of the large spread.

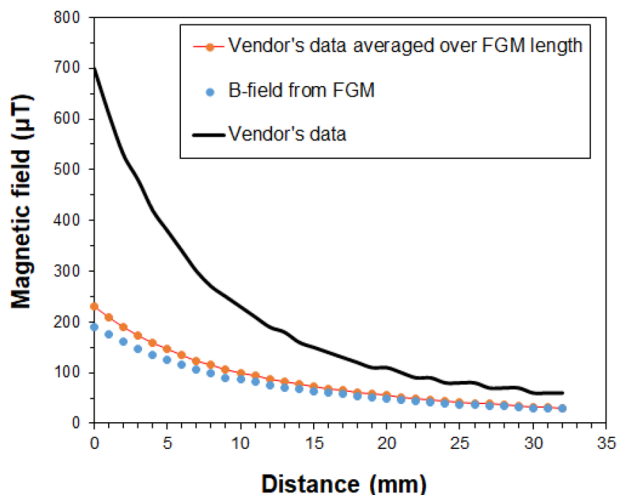| Sensor type	Sensitivity at 2 K	Sensitivity linearity error (%)	Sensitivity temperature coefficient (1/K)	Offset voltage at 2 K	Offset voltage temperature coefficient (μV/K)
HP	96 ± 2 nV/μT	0.6	$(-4.6 \pm 2.5) \times 10^{-3}$	-22 ± 176 μV	0.05 ± 0.24
AMR	35.3 ± 0.8 μV/μT/V	0.3	$(-1.0 \pm 0.4) \times 10^{-3}$	$(-3.5, 3.6)$ mV	$(-44, 15)$

FIG. 4. Magnetic field along the axis of a small cylindrical permanent magnet provided by the vendor as a function of the distance from one of the poles (solid line), in comparison to the data measured with the FGM and the vendor's data averaged over the 28 mm length of the FGM core.

B. Sensors performance in the MFSS

The prototype version of the MFSS was assembled on a TESLA-shaped,[35] 1.3 GHz single-cell SRF cavity made of bulk Nb. Four sensors can be mounted on two brackets, 180° apart, which can rotate one full turn around the cavity. The sensors are held in contact with the cavity surface by small springs. Figure 5 shows a schematic of the sensors' location and their angle with respect to the cavity axis. The cavity with the MFSS is attached to a vertical test stand, inserted in a vertical cryostat, 71 cm in diameter, 275 cm deep. The Earth's field is shielded inside the cryostat by a combination of a μ-metal shield and a compensation coil wound around the shield. The current from a DC power supply connected to the compensation coil can be adjusted to vary the residual magnetic field in the cryostat. In the first experiment, four calibrated HP and AMR sensors were used. In a second experiment, four FGMs replaced the AMR sensors. The sensors' instrumentation and data acquisition parameters used for the MFSS were the same as those used for the sensors' calibration. A program written in LabVIEW was used for instruments' control and data acquisition such that the magnetic field was measured sequentially from each sensor. It takes ~1.6 s to acquire four data points from one HP and ~1.2 s to acquire the same number of samples from one AMR sample, with the chosen data acquisition settings, and therefore, the time interval between two subsequent measurements from each sensor is ~11.2 s. A time interval of ~19 s between two consecutive measurements with the same sensor occurred for the setup with AMR sensors and FGMs because a settling time of ~3 s was necessary after switching from one FGM to the next, even though the acquisition time for four samples from one FGM was only ~0.5 s. Figures 6 and 7 show the magnetic field as a function of time measured at a fixed location and fixed residual ambient magnetic field with each type of sensor, in order to evaluate the overall resolution. The magnitude measured by each sensor is different because of the different orientation, as shown in Fig. 5, with respect to the applied magnetic field. For each type of sensor,
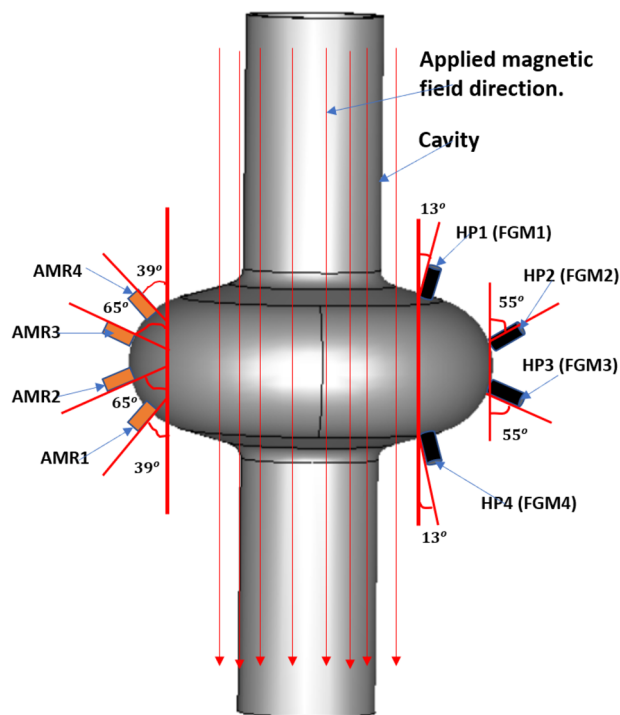

FIG. 5. Schematic diagram of the trapped flux measurement setup. FGMs replaced the HPs in one set of measurements.

we consider the average value of the standard deviation obtained from the measurement of $B_a(t)$ with four sensors to be the resolution of that sensor in our setup. Such a resolution was measured to be 65 nT for the HP, 75 nT for AMR sensors, and 18 nT for the FGM.
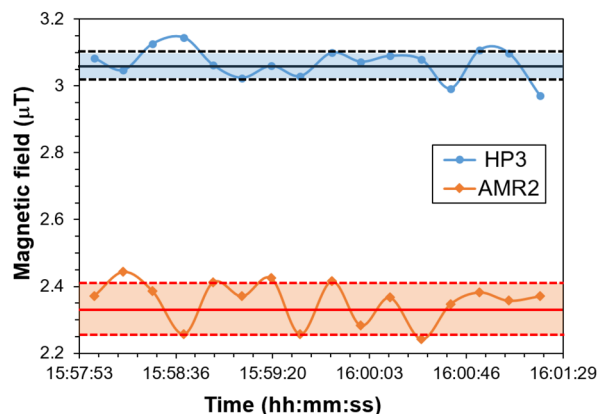

FIG. 6. Ambient magnetic field at 14 K measured over time with HP3 and AMR2 sensors kept at a fixed location in the MFSS. The solid lines are the average values, and the shaded areas between dashed lines are $\pm 1\sigma$. The different magnitude of the magnetic field measured by the sensors is due to their different orientation with respect to the ~5 μT applied field.
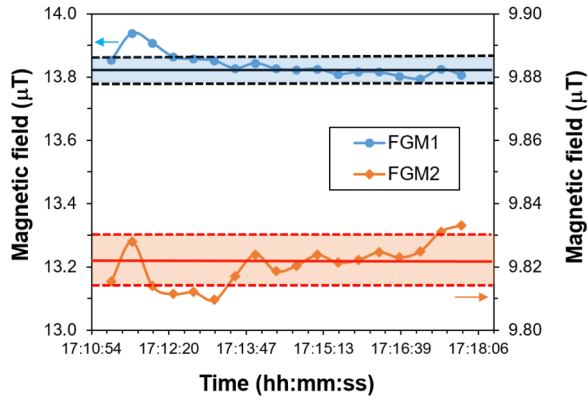
FIG. 7. Ambient magnetic field at 75 K measured over time by two FGM sensors kept at a fixed location in the MFSS. The solid lines are the average values, and the shaded areas between dashed lines are $\pm 1\sigma$. The different magnitude of the magnetic field measured by the sensors is due to their different orientation with respect to the $\sim 16~\mu$T applied field.

IV. ESTIMATED SENSITIVITY TO TRAPPED FLUX

A pinned vortex in a superconductor generates the induction of a monopole field outside a superconductor,[17]

$$\vec{B} = \frac{\Phi_0}{2\pi r^2}\hat{r}, \tag{1}$$

where $\vec{r}$ is a radial vector connecting the tip of the vortex and the observation point, and $\Phi_0 = h/2e$ is the magnetic flux quantum.

Considering the surface of a superconductor occupying the xy plane, with a vortex at the origin, the geometry of the three types of sensors is shown schematically in Fig. 8. For the HP, the magnetic flux Φ_z through a square area of side $d = 50~\mu$m, oriented parallel to the xy plane and centered at $\vec{r} = z\hat{z}$ above the origin, is given by

$$\Phi_z = \frac{2\Phi_0}{\pi}\tan^{-1}\left(\frac{d^2}{2z\sqrt{2d^2 + 4z^2}}\right). \tag{2}$$

The minimum number of trapped vortices N_{HP} that could be measured with the HP as a function of the distance from the superconductor's surface can be estimated as

$$N_{HP} = B_{HP}d^2/\Phi_z, \tag{3}$$

where $B_{HP} = 65$ nT is the resolution of the HP. For the AMR sensor, the average magnetic field over a square plane of size $a = 0.75$ mm perpendicular to the superconductor's surface and centered at $\vec{r} = z\hat{z}$ above a vortex at the origin is given by

$$B_{avg} = \frac{1}{a^2}\int_z^{a+z}\int_{-a/2}^{a/2} B(r)\,dx\,dz = \frac{\Phi_0}{2\pi a^2}\ln\left[\frac{(\alpha+1)(\beta-1)}{(\beta+1)(\alpha-1)}\right], \tag{4}$$

where $\alpha = \sqrt{1 + 4(z/a)^2}$ and $\beta = \sqrt{1 + 4(1 + z/a)^2}$. The minimum number of trapped vortices N_{AMR} that could be measured with the
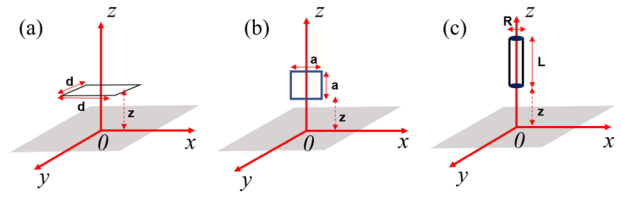

FIG. 8. Schematic representation of a HP (a), AMR sensor (b), and FGM (c) positioned at a distance z above a trapped vortex at the origin, inside a superconductor with the surface on the xy-plane.

AMR sensor can be estimated as

$$N_{AMR} = B_{AMR}/B_{avg}, \tag{5}$$

where $B_{AMR} = 75$ nT is the AMR sensor's resolution.

Finally, for the case of the FGM, the magnetic flux over a circular area of radius $R = 0.5$ mm parallel to the superconductor's surface, centered at $\vec{r} = z\hat{z}$ above a vortex at the origin, is given by

$$\Phi_z = \Phi_0\left(1 - \frac{z}{\sqrt{d^2 + z^2}}\right). \tag{6}$$

The average flux over the length of the sensor's core, $L = 28$ mm, can be calculated as

$$\langle\Phi_z\rangle = \frac{1}{L}\int_z^{z+L}\Phi(z)\,dz$$
$$= \Phi_0\left\{1 - \frac{R}{L}\left[\sqrt{1 + \left(\frac{z+L}{R}\right)^2} - \sqrt{1 + \left(\frac{z}{R}\right)^2}\right]\right\}, \tag{7}$$

where $R = 0.5$ mm is the core radius. The minimum number of trapped vortices N_{FGM} that could be measured with the FGM as a function of the distance from the superconductor's surface can be estimated as

$$N_{FGM} = B_{FGM}\pi R^2/\langle\Phi_z\rangle, \tag{8}$$

where $B_{FGM} = 18$ nT is the FGM's resolution. Figure 9 shows the minimum number of trapped vortices that could be measured with each type of sensor as a function of the distance from the superconductor's surface, starting at the minimum distance from the surface allowed for each sensor.

Initial measurements with the prototype MFSS were made after the cavity was cooled in an $\sim 10~\mu$T residual field. The temperature gradient between the cavity irises, measured with calibrated Cernox resistance temperature devices (RTDs), was ~ 20 K when the bottom RTD reached 9.2 K. Figure 10 shows the results from a full scan around the cavity for sensor HP4 at 4.4 K, showing two peaks, at $80°$ and at $130°$. The data were reproduced several times, after multiple thermal cycling to 300 K. Such peaks were not detected when scanning with AMR or FGM probes. The total scan time with four HPs and four FGMs was ~ 13 min. The amplitude of the peak at $130°$ was $B_v \sim 7~\mu$T above the uniform $\sim 9~\mu$T residual field. The number of trapped vortices can be estimated as $N = B_v d^2/\Phi_z$, where Φ_z is calculated using Eq. (2), resulting in ~ 320 vortices with mean spacing $l_v = d/\sqrt{N} = 2.8~\mu$m.
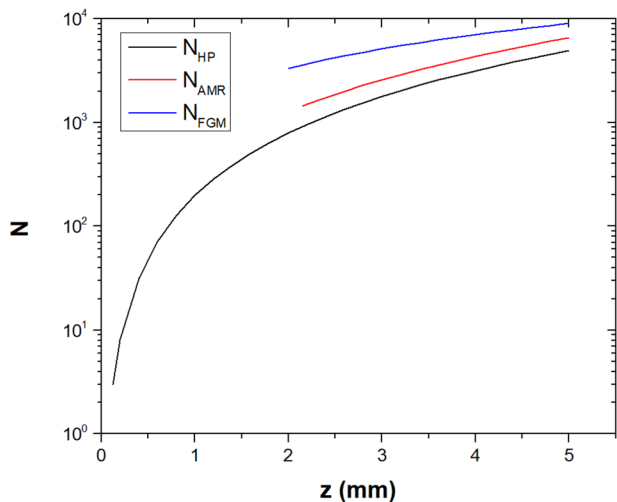
FIG. 9. Minimum number of trapped vortices calculated for each type of sensor as a function of the distance between the cavity surface and the sensor, starting at the minimum physical distance for each sensor.

V. DISCUSSION

All three types of magnetic field sensors have pros and cons: the HP and the FGMs are significantly more expensive than the AMR sensors, the AMR sensor requires two more wires per sensor than the HP and FGM, the FGM has the highest magnetic field resolution, and it does not require an independent calibration, but it has a large size. The feature of a magnetic field sensor that is most useful in a setup to detect trapped flux in an SRF cavity is the ability to detect the smallest number of a bundle of trapped vortices. Figure 9 shows that the HP is the best sensor in that respect and the FGM the worst. The surface resistance due to N sparse vortices per unit area, n_v, under an RF field at GHz frequencies is given by[4]

$$R_i = n_v (2\pi)^{3/2} \lambda \xi \frac{\sqrt{\mu_0 f \rho_n}}{\ln\left(\frac{\lambda}{\xi} + \frac{1}{2}\right)^{1/2}}, \qquad (9)$$
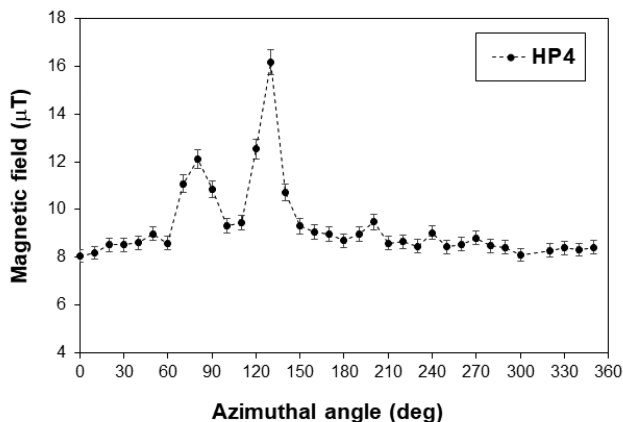

FIG. 10. Residual magnetic field at 4.4 K as a function of the azimuthal angle around the cavity measured with HP4.

where λ is the RF penetration depth, ξ is the coherence length, f is the RF frequency, and ρ_n is the normal-state resistivity. The number of trapped vortices, N, that might be relevant for SRF cavities could be estimated using Eq. (9) considering, as an example, a local surface resistance $R_i = 1\ \mu\Omega$, about a factor of 100 greater than the BCS surface resistance at the same frequency at 2 K, over a $100 \times 100\ \mu m^2$ area. Considering $\lambda = \xi = 40$ nm for clean Nb, $\rho_n = 1.5 \times 10^{-9}\ \Omega m$, and $f = 1.3$ GHz, the total number of trapped vortices is ~180.

The results shown in Fig. 10 indicate that the cryogenic HP has the capability to detect such amounts of trapped vortices. The main issues with using the HP sensors are their fragility and comparatively low sensitivity, which require careful measurements of the sensors' offset voltage. We did not pursue yet the development of a suitable magnetic field concentrator to place between the cavity surface and the sensor to enhance the sensitivity as the data acquisition module seems adequate for an accurate measurement of voltages of the order of tens of nanovolts. AMR sensors are selected as the second type of sensors to be installed in the MFSS and are planned to be used for the initial scan of the surface at a lower spatial resolution to identify possible regions with trapped flux, which can then be scanned with greater resolution using the HPs.

VI. CONCLUSION

Three types of magnetic field sensors have been evaluated to detect trapped vortices at the surface of SRF cavities. HPs have the smallest sensing area and can be placed the closest to the cavity surface, resulting in the lowest minimum number of detectable vortices. The initial results obtained with the prototype MFSS mounted on a single-cell Nb cavity showed the ability of the HP to measure a bundle of a few hundred trapped vortices, which can produce appreciable RF losses in an SRF cavity. The fabrication of the full-scale version of the MFSS is in progress. The full-scale system will have 8 HPs and 16 AMR sensors along the profile of a single-cell cavity, with improved wiring and reduced scan time.

AUTHOR DECLARATIONS

Conflict of Interest

The authors have no conflicts to disclose.

DATA AVAILABILITY

The data that support the findings of this study are available from the corresponding author upon reasonable request.

REFERENCES

[1]H. Padamsee, J. Knobloch, and T. Hays, *RF Superconductivity for Accelerator* (Wiley & Sons, New York, 1998).

[2] A. Gurevich, "Theory of RF superconductivity for resonant cavities," Supercond. Sci. Technol. **30**, 034004 (2017).

[3] D. C. Mattis and J. Bardeen, "Theory of the anomalous skin effect in normal and superconducting metals," Phys. Rev. **111**, 412–417 (1958).

[4] A. Gurevich and G. Ciovati, "Effect of vortex hotspots on the radio-frequency surface resistance of superconductors," Phys. Rev. B **87**, 054502 (2013).

[5] A. Gurevich and G. Ciovati, "Dynamics of vortex penetration, jumpwise instabilities, and nonlinear surface resistance of type-II superconductors in strong rf fields," Phys. Rev. B **77**, 104501 (2008).

[6] D. B. Liarte, D. Hall, P. N. Koufalis, A. Miyazaki, A. Senanian, M. Liepe, and J. P. Sethna, "Vortex dynamics and losses due to pinning: Dissipation from trapped magnetic flux in resonant superconducting radio-frequency cavities," Phys. Rev. Appl. **10**, 054057 (2018).

[7] W. P. M. R. Pathirana and A. Gurevich, "Nonlinear dynamics and dissipation of a curvilinear vortex driven by a strong time-dependent Meissner current," Phys. Rev. B **101**, 064504 (2020).

[8] W. P. M. R. Pathirana and A. Gurevich, "Effect of random pinning on nonlinear dynamics and dissipation of a vortex driven by a strong microwave current," Phys. Rev. B **103**, 184518 (2021).

[9] T. Kubo, "Flux trapping in superconducting accelerating cavities during cooling down with a spatial temperature gradient," Prog. Theor. Exp. Phys. **2016**, 053G01.

[10] A. Romanenko, A. Grassellino, O. Melnychuk, and D. A. Sergatskov, "Dependence of the residual surface resistance of superconducting radio frequency cavities on the cooling dynamics around T_c," J. Appl. Phys. **115**, 184903 (2014).

[11] P. Dhakal and G. Ciovati, "Effect of cooldown and residual magnetic field on the performance of niobium–copper clad superconducting radio-frequency cavity," Supercond. Sci. Technol. **31**, 015006 (2017).

[12] J.-M. Vogt, O. Kugeler, and J. Knobloch, "Impact of cool-down conditions at T_c on the superconducting rf cavity quality factor," Phys. Rev. Spec. Top.–Accel. Beams **16**, 102002 (2013).

[13] M. Martinello, M. Checchin, A. Grassellino, A. C. Crawford, O. Melnychuk, A. Romanenko, and D. A. Sergatskov, "Magnetic flux studies in horizontally cooled elliptical superconducting cavities," J. Appl. Phys. **118**, 044505 (2015).

[14] S. Huang, T. Kubo, and R. L. Geng, "Dependence of trapped-flux-induced surface resistance of a large-grain Nb superconducting radio-frequency cavity on spatial temperature gradient during cooldown through T_c," Phys. Rev. Accel. Beams **19**, 082001 (2016).

[15] S. Posen, M. Checchin, A. C. Crawford, A. Grassellino, M. Martinello, O. S. Melnychuk, A. Romanenko, D. A. Sergatskov, and Y. Trenikhina, "Efficient expulsion of magnetic flux in superconducting radiofrequency cavities for high Q_0 applications," J. Appl. Phys. **119**, 213903 (2016).

[16] P. Dhakal, G. Ciovati, and A. Gurevich, "Flux expulsion in niobium superconducting radio-frequency cavities of different purity and essential contributions to the flux sensitivity," Phys. Rev. Accel. Beams **23**, 023102 (2020).

[17] J. R. Kirtley, "Fundamental studies of superconductors using scanning magnetic imaging," Rep. Prog. Phys. **73**, 126501 (2010).

[18] I. Parajuli, G. Ciovati, W. Clemens, J. Delayen, A. Gurevich, and J. Nice, "Design and commissioning of a magnetic field scanning system for SRF cavities," in Proc. SRF'19, International Conference on RF Superconductivity No. 19, Geneva, Switzerland, 2019, http://www.jacow.org, pp. 547–549.

[19] AREPOC s.r.o., HHP-VF Sensor Datasheet, 2008.

[20] D. F. He, M. Tachiki, and H. Itozaki, "Highly sensitive anisotropic magnetoresistance magnetometer for eddy-current nondestructive evaluation," Rev. Sci. Instrum. **80**, 036102 (2009).

[21] J. Včelák, P. Ripka, J. Kubík, A. Platil, and P. Kašpar, "AMR navigation systems and methods of their calibration," Sens. Actuators, A **123-124**, 122–128 (2005).

[22] K. Allweins, M. von Kreutzbruck, and G. Gierelt, "Defect detection in aluminum laser welds using an anisotropic magnetoresistive sensor array," J. Appl. Phys. **97**, 10Q102 (2005).

[23] M. H. Kang, B. W. Choi, K. C. Koh, J. H. Lee, and G. T. Park, "Experimental study of a vehicle detector with an AMR sensor," Sens. Actuators, A **118**, 278–284 (2005).

[24] G. Martinet, "Characterization of small AMR sensors in liquid helium to measure residual magnetic field on superconducting samples," in Proc. SRF'19, International Conference on RF Superconductivity No. 19, Geneva, Switzerland, 2019, http://www.jacow.org, pp. 576–579.

[25] T. Okada, E. Kako, T. Konomi, M. Masuzawa, H. Sakai, K. Tsuchiya, R. Ueki, K. Umemori, P. Pizzol, A. Poudel et al., "Systematic evaluation of magnetic sensitivities of anisotropic magnetoresistive sensors at liquid helium temperature for superconducting cavities," Rev. Sci. Instrum. **92**, 035003 (2021).

[26] R. Ueki, T. Okada, M. Masuzawa, K. Tsuchiya, T. Kawamoto, K. Umemori, E. Kako, T. Konomi, and H. Sakai, "Study on magneto-resistance sensors for low magnetic field measurements," IEEE Trans. Appl. Supercond. **30**, 1–4 (2020).

[27] B. Schmitz, J. Köszegi, K. Alomari, O. Kugeler, and J. Knobloch, "Magnetometric mapping of superconducting RF cavities," Rev. Sci. Instrum. **89**, 054706 (2018).

[28] T. Okada, E. Kako, T. Konomi, M. Masuzawa, A. Poudel, H. Sakai, T. Tajima, K. Tsuchiya, R. Ueki, and K. Umemori, "Development of temperature and magnetic field mapping system for superconducting cavities at KEK," in Proc. SRF'19, International Conference on RF Superconductivity No. 19, Geneva, Switzerland, 2019, http://www.jacow.org, pp. 583–585.

[29] S. Lobo, M. Liepe, and T. Oseroff, "Magnetic field mapping system for cornell sample host cavity," in Proc. SRF'19, International Conference on RF Superconductivity No. 19, Geneva, Switzerland, 2019, http://www.jacow.org, pp. 961–963.

[30] F. Kramer, O. Kugeler, J.-M. Köszegi, and J. Knobloch, "Impact of geometry on flux trapping and the related surface resistance in a superconducting cavity," Phys. Rev. Accel. Beams **23**, 123101 (2020).

[31] AFF755B, Magnetoresistive field sensor, Sensitec GmbH, Georg-Ohm-Str. 11, 35633, Lahnau, Germany, 2018.

[32] Bartington Instruments Ltd., Mag-01h datasheet, https://www.bartington.com/mag-01h/ (2017); accessed 25 June 2021.

[33] C. Elliott, V. Vijayakumar, W. Zink, and R. Hansen, "National instruments LabVIEW: A programming environment for laboratory automation and measurement," J. Assoc. Lab. Autom. **12**, 17–24 (2007).

[34] S. Sanfilippo, "Hall probes: Physics and application to magnetometry," in CAS 2009–CERN Accelerator School: Magnets, Proceedings, 2011.

[35] B. Aune, R. Bandelmann, D. Bloess, B. Bonin, A. Bosotti, M. Champion, C. Crawford, G. Deppe, B. Dwersteg, D. A. Edwards, H. T. Edwards, M. Ferrario, M. Fouaidy, P.-D. Gall, A. Gamp, A. Gössel, J. Graber, D. Hubert, M. Hüning, M. Juillard, T. Junquera, H. Kaiser, G. Kreps, M. Kuchnir, R. Lange, M. Leenen, M. Liepe, L. Lilje, A. Matheisen, W.-D. Möller, A. Mosnier, H. Padamsee, C. Pagani, M. Pekeler, H.-B. Peters, O. Peters, D. Proch, K. Rehlich, D. Reschke, H. Safa, T. Schilcher, P. Schmüser, J. Sekutowicz, S. Simrock, W. Singer, M. Tigner, D. Trines, K. Twarowski, G. Weichert, J. Weisend, J. Wojtkiewicz, S. Wolff, and K. Zapfe, "Superconducting TESLA cavities," Phys. Rev. Spec. Top.–Accel. Beams **3**, 092001 (2000).